Infrared spectroscopy and nano-imaging of the insulator-to-metal transition in vanadium dioxide

M. M. Qazilbash,[1,*] M. Brehm,[2] G. O. Andreev,[1] A. Frenzel,[1] P.-C. Ho,[1,3] Byung-Gyu Chae,[4] Bong-Jun Kim,[4] Sun Jin Yun,[4] Hyun-Tak Kim,[4], A. V. Balatsky,[5] O. G. Shpyrko,[1] M. B. Maple,[1] F. Keilmann,[2] and D. N. Basov[1]

[1] *Physics Department, University of California-San Diego, La Jolla, California 92093, USA.*

[2] *Abt. Molekulare Strukturbiologie, Max-Planck-Institut für Biochemie and Center for NanoScience, 82152 Martinsried, München, Germany.*

[3] *Department of Physics, California State University-Fresno, Fresno, California 93740, USA.*

[4] *IT Convergence and Components Lab, Electronics and Telecommunications Research Institute (ETRI), Daejeon 305-350, Korea.*

[5] *Theoretical Division and Center for Integrated Nanotechnologies, MS B262, Los Alamos National Laboratory, Los Alamos, New Mexico 87545, USA.*

(Dated: February 21, 2024)

We present a detailed infrared study of the insulator-to-metal transition (IMT) in vanadium dioxide (VO_2) thin films. Conventional infrared spectroscopy was employed to investigate the IMT in the far-field. Scanning near-field infrared microscopy directly revealed the percolative IMT with increasing temperature. We confirmed that the phase transition is also percolative with cooling across the IMT. We present extensive near-field infrared images of phase coexistence in the IMT regime in VO_2. We find that the coexisting insulating and metallic regions at a fixed temperature are static on the time scale of our measurements. A novel approach for analyzing the far-field and near-field infrared data within the Bruggeman effective medium theory was employed to extract the optical constants of the incipient metallic puddles at the onset of the IMT. We found divergent effective carrier mass in the metallic puddles that demonstrates the importance of electronic correlations to the IMT in VO_2. We employ the extended dipole model for a quantitative analysis of the observed near-field infrared amplitude contrast and compare the results with those obtained with the basic dipole model.

PACS numbers: 71.30.+h, 71.27.+a, 78.20.-e, 78.30.-j

arXiv:0904.0294v1 [cond-mat.str-el] 2 Apr 2009

I. INTRODUCTION

Vanadium dioxide (VO_2) undergoes an insulator-to-metal transition (IMT) at $T_c \approx 340$ K. The IMT is accompanied by a change of lattice structure from a monoclinic ($M1$) unit cell in the low-temperature insulating phase to tetragonal (rutile) symmetry in the metallic phase. VO_2 has been studied extensively for two main reasons. First, the driving mechanism of the IMT has remained controversial and many experimental and theoretical studies have focused on understanding it.[1,2] Secondly, VO_2 has immense potential for applications[3,4,5] because the phase transition occurs only 40 K above room temperature and involves dramatic changes in transport, infrared and optical properties. Moreover, the phase transition can also be triggered optically[6,7] and electrically[4,8] leading to new optical and electronic devices.

The reason the driving mechanism of the IMT in VO_2 has been a subject of controversy is the complex nature of the interactions in this material. VO_2 consists of just two elements, vanadium and oxygen, with well-documented lattice structures in the M1 and rutile phases. The model of delocalized d-electrons of vanadium (one per vanadium ion) moving in the periodic potential created by the lattice was expected to explain the documented features of the IMT in VO_2. In the early literature, the phase transition in VO_2 was described in terms of the structural distortion that leads to the formation of vanadium pairs and unit-cell doubling.[9] This Peierls instability was thought to occur due to the coupling of the conduction electrons to a soft phonon mode of vanadium.[10,11,12] However, the model of a Peierls instability within band theory alone [13,14] cannot satisfactorily explain several experimental aspects of the phase transition and the properties of the insulating and metallic phases existing in its vicinity. Following are a few examples of such experimental observations: the ≈ 0.6 eV energy gap in the $M1$ insulator measured by infrared and photoemission techniques[15,16,17,18,19]; the changes in optical conductivity and spectral weight up to at least 6 eV due to the IMT[15,16,17,18,19]; the satellite feature at ≈ 1 eV below the Fermi energy seen in photoemission in the rutile metal which may well be a remnant of the lower Hubbard band[20]; and lack of resistivity saturation in the rutile metal beyond the Ioffe-Regel-Mott limit of metallic transport which is difficult to explain within a framework based on electron-phonon coupling.[18,21,22] There is growing evidence that electron-electron correlations cannot be neglected in any viable description of the IMT in VO_2.[18,19,23,24,25,26,27] Several previous theoretical studies have emphasized the role of electronic correlations.[28,29,30,31,32]

It appears that the interplay among various electronic degrees of freedom (charge, orbital and spin) and their coupling to the lattice degrees of freedom (phonons) leads to complex behavior in VO_2. This is a hallmark of many transition-metal oxides that exhibit remark-

able properties like high-temperature superconductivity, colossal magnetoresistance and multiferroicity.[33] Many of these transition metal oxides have a rich phase diagram with a diversity of phases.[33] Some of the exotic properties may well be due to phase coexistence close to phase boundaries. Recent experimental work on high-temperature superconductors and manganites provides direct evidence of phase separation and inhomogeneity in these materials on mesoscopic and nanoscopic length scales.[34,35,36,37,38,39] It is thought that competing electronic and phononic degrees of freedom lead to phase separation and a multiplicity of phases in transition metal oxides.[33] The evolution of one phase to another appears to proceed on the nanometer scale leading to phase coexistence and inhomogeneity. This motivated us to investigate the IMT regime in VO_2 on the nanometer length scales with the pioneering technique of scattering scanning near-field infrared microscopy (s-SNIM).[40]

While the IMT in VO_2 has been studied previously by far-field infrared and THz techniques[41,42], our studies combine far-field infrared spectroscopy with near-field infrared imaging.[23] With s-SNIM, we have imaged the evolution of the thermally-induced IMT in a thin film of VO_2. We found that the VO_2 film underwent a percolative transition with increasing temperature across the IMT. We analyzed the s-SNIM data along with the far-field infrared spectroscopy data within the Bruggeman effective medium theory (EMT), and discovered that the metallic islands embedded in the insulating host exhibit divergent effective mass which is evidence of the Mott transition within the Brinkman-Rice framework.[23,43,44] In this paper, we further discuss the underlying physics of the IMT in VO_2. We present extensive s-SNIM images obtained while heating and cooling across the IMT which confirm the reproducibility of our results. We demonstrate the static nature of the coexisting insulating and metallic regions over many minutes at a fixed temperature. A quantitative discussion of the observed near-field infrared amplitude contrast in the IMT regime is included. The amplitude contrast was modeled with the so-called dipole description[40] and its refined version. Moreover, we explore the novel approach to data analysis of the far-field and near-field infrared data within the Bruggeman effective medium theory and expound upon the merits and limitations of this procedure.

This article is divided into several sections. The details of the sample preparation and characterization are given in the next section. The far-field infrared spectroscopy experiments and data analysis are described in Section III. This is followed by a description of the s-SNIM technique and presentation of the data in Sections IV and V respectively. The data analysis within the Bruggeman effective medium theory is described in Section VI. This is followed by a Summary and Outlook Section and three appendices.

II. SAMPLES

VO_2 films about 100 nm thick were grown on $(\bar{1}012)$ oriented sapphire (Al_2O_3) substrates by the sol gel method. The details of growth and characterization are given in Ref. 45. In Fig. 1a we present the X-ray diffraction data on the VO_2 film which shows that the film is single phase $M1$-VO_2 with (200) orientation. The resistance of the film was measured by a standard four-probe method, and the data is displayed in Fig. 1b. The film undergoes a first-order, hysteretic IMT with four orders of magnitude change in the resistance. We chose thin films of VO_2 for infrared measurements in the phase transition regime instead of single crystals because the IMT is destructive for VO_2 crystals [46] leading to potential problems of reproducibility and significant uncertainties in the quantitative results in the phase transition regime. Data obtained for high quality films grown on lattice matched substrates are free of the above complications and thus enable studies of the intrinsic properties of VO_2. Our VO_2 films do not show signs of deterioration even after going through several cycles across the IMT. This was verified by repeated resistance measurements of the IMT, and by ellipsometric and reflectance experiments that give reproducible data in the insulating and metallic phases before and after cycling through the IMT.

III. FAR-FIELD INFRARED SPECTROSCOPY

Spectroscopic ellipsometry provides the ellipsometric coefficients ($\Psi(\omega)$ and $\Delta(\omega)$) at each measured frequency.[47] This enables us to obtain the optical constants of the VO_2 film without recourse to Kramers-Kronig analysis which may not be applicable in the IMT regime of VO_2 because of inhomogeneity and phase-coexistence. Provided the incident wavelength is large compared to the size of the inhomogeneities, the inhomogeneous system can be described by an effective dielectric function[48]. This is certainly expected to be the case for long wavelengths in the far- and mid-infrared regime (between 40 cm^{-1} and 5000 cm^{-1}). Furthermore, we find that in accord with the EMT[48], weighted averaging of the dielectric functions of the insulating phase and rutile metallic phase at shorter wavelengths (higher frequencies) adequately describes the data (see Appendix A). Therefore, it is appropriate to assign an effective dielectric function to the inhomogeneous, phase-separated regime of VO_2 even when the wavelength becomes comparable to the size of the metallic puddles. The effective dielectric function of the inhomogeneous, phase-separated regime of VO_2 is thus obtained via the standard analysis of the combined ellipsometric and reflectance data based on a two-layer model of a VO_2 film on a sapphire substrate.[19,47] The ellipsometric data spanned the frequency range 400 - 20000 cm^{-1}, and near-normal incidence reflectance covered the frequency range 40 - 680 cm^{-1}.

We note that in general, the complex dielectric function $\tilde{\epsilon}(\omega)= \epsilon_1(\omega) + i\epsilon_2(\omega)$ of a material is related to the complex conductivity $\tilde{\sigma}(\omega)= \sigma_1(\omega) + i\sigma_2(\omega)$ by the following equation:

$$\tilde{\epsilon}(\omega) = 1 + \frac{4\pi i}{\omega}\tilde{\sigma}(\omega) \quad (1)$$

The real part of the optical conductivity $\sigma_1(\omega)$ is plotted in Fig. 1c as a function of frequency (ω) for representative temperatures in the IMT regime of VO_2. The inset in Fig. 1c shows the temperature-dependence of the real part of the dielectric function $\epsilon_1(\omega = 50\ \mathrm{cm}^{-1})$ in the IMT regime. Fig. 1d and its inset show $\sigma_1(\omega)$ and $\epsilon_1(\omega = 50\ \mathrm{cm}^{-1})$ respectively with phonon contributions subtracted. The contributions of VO_2 phonons to the dielectric functions were modeled by Lorentzian oscillators and subsequently subtracted so that the electronic contribution to the optical constants could be unambiguously presented and analyzed.

An optical gap of $\approx 4000\ \mathrm{cm}^{-1}$ (0.5 eV) is evident in $\sigma_1(\omega)$ of the insulating phase (295 K $\leq T \leq$ 341 K). As the VO_2 film enters the IMT regime for $T >$ 341 K, the conductivity in the gap increases and gradually fills the gap. The first inter-band transition centered at $10500\ \mathrm{cm}^{-1}$ does not appear to shift to lower frequencies as would be expected if the gap were to collapse. The filling up of the optical gap, rather than a collapse, is also seen in other correlated (or Mott) insulators like the cuprates that are rendered conducting through chemical doping.[2,49,50] In addition, we observe an isosbestic point in $\sigma_1(\omega)$ characterized by invariant conductivity (depicted by an open circle in Fig. 1c,d). The isosbestic point is also seen in other Mott systems[51] although its significance is yet to be understood. The observations discussed in the preceding sentences point to the importance of electronic correlations in VO_2. As the temperature is increased, the low frequency conductivity increases until the film becomes fully metallic as seen from the broad Drude-like feature at $T = 360$ K. We note that the enhanced spectral weight at low energies as the film becomes increasingly metallic is borrowed from higher lying inter-band transitions.[17,18,19] The divergence of ϵ_1 shown in the insets of Fig. 1c,d is similar to that known from percolative insulator-to-metal transitions where it occurs due to enhanced capacitive coupling between the metallic regions as they grow and proliferate in the insulating host.[41,52] ϵ_1 abruptly becomes negative at $T = 343$ K signaling that the metallic regions have percolated (connected) forming a macroscopic conducting path for the charge carriers.

IV. SCANNING NEAR-FIELD INFRARED MICROSCOPY

The characteristic evolution of the effective area-averaged optical constants in the IMT regime of VO_2 provides indirect evidence of a percolative phase transition with coexisting insulating and metallic regions. Our objective was to directly observe the percolation with scanning near-field optical techniques. We chose to directly image the IMT with s-SNIM at the mid-infrared frequency of $930\ \mathrm{cm}^{-1}$. As can be seen from Fig. 1c,d, the optical conductivity of the insulating and metallic phases of VO_2 is very different at this frequency and so a large contrast is expected in the near-field amplitude signal.

Scattering scanning near-field infrared microscopy was performed with a custom Atomic Force Microscope (AFM) using Pt-coated silicon tips in the tapping mode.[40,53] The $\omega = 930\ \mathrm{cm}^{-1}$ infrared frequency was provided by a CO_2 laser. The pseudo-heterodyne scheme with second harmonic demodulation was employed to isolate and detect the near-field amplitude signal.[54] The spatial resolution of the near-field infrared probe is typically 10-20 nm and is set by the radius of curvature of the tip. The near-field penetrates about 20 nm into the VO_2 film and can therefore be considered a bulk probe of the insulator-to-metal transition.[55]

The near-field interaction between the tip and the sample is described by the dipole model. This is the simplest model that quantitatively describes the near-field interaction and has been found to be accurate in some cases.[40] Within this model, the complex scattered signal at the second harmonic of the tapping frequency Ω is a function of the optical constants of the tip and the sample.[40] The incident infrared light polarizes the tip and within the dipole model, it is sufficient to model the polarizability of the tip with an effective spherical dipole of radius a (≈ 20 nm). The interaction between the tip dipole and the sample is modeled by considering a mirror dipole in the sample whose polarizability depends on the local optical constants of the sample in the region directly below the tip. The effective polarizability of the interacting tip-sample system (α_{eff}) is given by:

$$\alpha_{eff} = \frac{\alpha(1+\beta)}{1 - \frac{\alpha\beta}{16\pi(a+z(t))^3}}. \quad (2)$$

α_{eff} is complex-valued and relates the incident E_i and scattered E_s electric fields via $E_s \propto \alpha_{eff}E_i$. The polarizability of the tip α is given by $\alpha = 4\pi a^3(\tilde{\epsilon}_t - 1)/(\tilde{\epsilon}_t + 2)$ where $\tilde{\epsilon}_t$ is the complex dielectric function of the tip at the incident laser frequency. The polarizability of the mirror dipole in the sample is given by $\alpha\beta$ where $\beta = (\tilde{\epsilon}_s - 1)/(\tilde{\epsilon}_s + 1)$ expresses the local dielectric response of the sample that depends on its complex dielectric function $\tilde{\epsilon}_s$ at the incident laser frequency.

The effective polarizability of the tip-sample system is a non-linear function of the tip-sample distance z. The tip-sample distance varies sinusoidally with time $z(t) = z_0(1+\cos(\Omega t))$ due to oscillation of the tip. In the tapping mode, the tip oscillates with an amplitude z_0 of about 40 nm at a frequency $\Omega = 25$ kHz. Therefore, the

effective polarizability and hence the near-field signal is modulated at harmonics of Ω.

$$\alpha_{eff} = (\alpha_{eff})_0 + (\alpha_{eff})_1 \cos(\Omega t) + (\alpha_{eff})_2 \cos(2\Omega t) + (\alpha_{eff})_3 \cos(3\Omega t) + ... + (\alpha_{eff})_n \cos(n\Omega t). \quad (3)$$

The nth harmonic coefficient of the near-field polarizability is as follows:

$$(\alpha_{eff})_n = \frac{\Omega}{2\pi} \int_{-\pi/\Omega}^{\pi/\Omega} \alpha_{eff} \cos(n\Omega t) dt. \quad (4)$$

Here α_{eff} is given by eq. 2. The nth harmonic of the scattered electric field $(E_s)_n = s_n e^{i\phi_n} \propto (\alpha_{eff})_n E_i$, where s_n and ϕ_n are the nth harmonic amplitude and phase coefficients respectively. Thus the second harmonic coefficient of the near-field amplitude s_2 can be calculated (up to a proportionality constant that can be calibrated) provided the complex dielectric functions of the tip and sample at the incident laser frequency are known.

More recently, it has been suggested that the $(1+\beta)$ term in the numerator of eq. 2 be replaced by the term $(1 + r)^2$, where r is the far-field Fresnel reflectance coefficient:[56,57,58]

$$\alpha_{eff} = \frac{\alpha(1+r)^2}{1 - \frac{\alpha\beta}{16\pi(a+z(t))^3}}. \quad (5)$$

In the above equation, the $(1 + r)^2$ term accounts for the indirect illumination of the tip from reflections at the sample surface.

The dielectric function $\tilde{\epsilon}_t$ of Pt at $\omega = 930$ cm^{-1} is $-1300 + 960i$.[59] The dielectric functions of VO_2 at $\omega = 930$ cm^{-1} are obtained from ellipsometric chracterization. These are as follows: 4.9 with negligibly small imaginary part for the monoclinic insulating phase, and $-35 + 119i$ for the rutile metallic phase. Therefore, the scattered near-field amplitude in the metallic phase of VO_2 is expected to be about twice that in the insulating phase from basic dipole model (eq. 2). However, the extended dipole model (eq. 5) gives a factor of 3 ratio for the near-field amplitudes in the metallic and insulating phases.

V. INFRARED NANO-IMAGING OF THE INSULATOR-TO-METAL TRANSITION IN VO_2

We now turn to Fig. 2 which displays the second harmonic amplitude images in the IMT regime of VO_2 obtained with s-SNIM at the incident laser frequency of 930 cm^{-1}. At $T = 341$ K, we observe an essentially uniform amplitude signal. As the temperature is increased, nanometer-scale regions with higher near-field amplitude appear. The increased near-field amplitude of these nano-scale puddles is due to their metallicity. The metallic puddles subsequently proliferate and grow in size, and then coalesce with increasing temperature. The $T = 360$ K near-field map shows higher near-field amplitude indicating that the scanned region has become completely metallic. Near-field amplitude images were also obtained while cooling the VO_2 film through the IMT and are shown in Appendix B. We note here that coexisting insulating and metallic domains in VO_2 nano-rods in the IMT regime have been observed with optical microscopy in Ref. 60. Moreover, the IMT at the surface of VO_2 films has also been imaged with scanning tunneling microscopy.[61]

The distribution of the scattered near-field amplitude for various temperatures in the IMT regime of VO_2 is plotted in Fig. 3a. This distribution is obtained from the images in Fig. 2. The asymmetry of the histograms and the presence of two peak structures are evidence of coexisting insulating and metallic phases in the IMT regime of VO_2. The peak at lower near-field amplitudes corresponds to the insulating phase and the one at higher amplitudes corresponds to the metallic phase. The median amplitude for the metallic phase at $T = 360$ K is about 15 times higher than the median amplitude for the insulating phase. This is far higher than the factor of 2-3 expected from the dipole model. While eq. 5 improves the description of the near-field contrast in our data compared to eq. 2, it still underestimates the contrast compared to experiment. A similar discrepancy between the measured near-field contrast and that predicted by the dipole model has also been noted for near-field terahertz measurements on the IMT in VO_2.[62]

We note that each of separate images in Fig. 2 has only a factor of 2-3 variation of the near-field amplitude contrast. Moreover, the median position of the "insulating" peak in Fig. 3a shows a small but noticeable increase with temperature without apparent reason. These observations led us to normalize the measured amplitude to the peak position of the insulating phase. The resulting distributions plotted as a function of the normalized amplitude are in fairly good agreement with the predictions of the dipole models (see Fig. 3b). The amplitude from the metallic phase is now a factor of 2-4 higher than that from the insulating phase. Note that the basic dipole model (eq. 2) gives better quantitative agreement in the regime with smaller sizes of the metallic puddles in the insulating host and vice versa. The extended dipole model (eq. 5) explains the data well in the regime where the insulating and metallic regions have similar length scales. The apparent continuous increase in the near-field amplitude of the metallic phase with increasing temperature (see Fig. 3a) and the 15 times higher near-field amplitude from the metallic phase compared to the insulating phase are phenomena that are not fully understood at present and require further investigation. The insulating and metallic fractions can, nevertheless be extracted from the near-field images and amplitude distributions as explained in the next section.

We note that the near-field images are repeatable when taken in five minute sequences over the same sample area and at a fixed temperature because they show nearly identical patterns of metallic puddles in the insulating host (see Appendix B). This indicates that the possible effect of dynamic fluctuations on the static patterns is small. This is discussed in detail in Appendix B.

VI. BROAD-BAND INFRARED RESPONSE OF THE METALLIC REGIONS IN THE PHASE COEXISTENCE REGIME OF VO_2

As shown in Appendix A, weighted averaging of optical constants of the insulating phase and of the rutile metallic phase within the Bruggeman effective medium theory (EMT) produces a good description of the far-field infrared data near the onset of the insulator-to-metal transition at high frequencies. Deviations from this description become progressively stronger at longer wavelengths, a regime where the EMT formalism is expected to be best applicable.[48] This implies that the optical constants of the metallic puddles when they first appear at the onset of the insulator-to-metal transition are different from the optical constants of the rutile metal at $T =$ 360 K. Therefore, we use the EMT to extract the optical constants of the metallic puddles.

Within the Bruggeman effective medium theory,[48] the effective (complex) optical constants $\tilde{\epsilon_E}(\omega)$ of a two-component inhomogeneous system are given by:

$$f\frac{\tilde{\epsilon_a}(\omega)-\tilde{\epsilon_E}(\omega)}{\tilde{\epsilon_a}(\omega)+\frac{1-q}{q}\tilde{\epsilon_E}(\omega)}+(1-f)\frac{\tilde{\epsilon_b}(\omega)-\tilde{\epsilon_E}(\omega)}{\tilde{\epsilon_b}(\omega)+\frac{1-q}{q}\tilde{\epsilon_E}(\omega)}=0 \quad (6)$$

In this equation, $\tilde{\epsilon_a}(\omega)$ and $\tilde{\epsilon_b}(\omega)$ are the complex optical constants of the metallic and insulating phases respectively, f and (1-f) are the volume fractions of the metallic and insulating phases respectively, and q is the depolarization factor that depends on the shape of the components which is inferred from near-field images. This factor is taken to be 0.2-0.4 assuming nearly spherical metallic regions at low concentrations of the newborn metallic state. This is because their lateral dimensions are less than the film thickness and the out-of-plane dimension is assumed to be similar to the lateral dimensions. The depolarization factor continuously increases to 0.5 (appropriate for thin flat disks) at higher concentrations of metallic clusters as their lateral dimensions exceed the out-of-plane dimension which is limited by the thickness of the film. The volume fractions of the insulating and metallic phases are obtained directly from the near-field images by fitting the amplitude distribution curves in Fig. 3a to two Gaussians, with the area under each Gaussian yielding the volume fraction of the respective phase. The optical constants of the insulating phase $\tilde{\epsilon_b}(\omega)$ and the inhomogeneous transition regime $\tilde{\epsilon_E}(\omega)$ have also been measured (see Fig. 1). The optical constants of the insulating phase are assumed to be independent of temperature in this analysis. Since $\tilde{\epsilon_E}(\omega)$, $\tilde{\epsilon_b}(\omega)$, and f are known whereas the range of q is constrained based on the knowledge of the metallic cluster size and film thickness, the equation can be solved to obtain the optical constants of the metallic regions $\tilde{\epsilon_a}(\omega)$, and hence the complex conductivity $\tilde{\sigma_a}(\omega)$ for each temperature. The real part of the conductivity $\sigma_{1a}(\omega)$ extracted by this procedure is plotted in Fig. 4(a) for representative temperatures in the IMT regime. The values of f and q used for the analysis are listed in Table I.

T (K)	f	q
342	0.18	0.2
342.6	0.31	0.33
343	0.48	0.45
343.6	0.7	0.5

TABLE I: The values of the filling fraction f and depolarization factor q used to obtain the optical constants of the metallic regions at selected temperatures within the framework of the EMT formalism.

We note that the form of $\sigma_{1a}(\omega)$ for the metallic regions that are separated by the insulating host exhibits a narrow Drude-like peak at low frequencies followed by a "dip-hump" structure at higher frequencies. This is quite different from $\sigma_{1a}(\omega)$ of the rutile metal at $T =$ 360 K which has a broad and featureless Drude peak. As the temperature is increased, and the metallic regions proliferate and grow, their $\sigma_{1a}(\omega)$ rapidly evolves to that seen in the rutile metallic phase. Here we note that the extracted optical constants of the metallic puddles at ω = 930 cm^{-1} are different from the optical constants of the $T = 360$ K rutile metal at this frequency. Nevertheless, within the dipole model (eqs.2 and 5), the near-field scattering amplitude at $\omega = 930$ cm^{-1} for the metallic puddles is expected to be nearly the same as that from the $T = 360$ K rutile metal.

Uncertainties in the magnitude of q do affect the behavior of the extracted spectra of the metallic puddles at the lowest frequencies accessible in our experiment. This is shown in Fig. 5. Changing q for a fixed value of f results in a variation in the $\sigma_1(\omega)$ spectra below 800 cm^{-1} whereas the variation is negligibly small above 800 cm^{-1}. We see that the mid-infrared band ("hump") peaked at $\approx$ 1800 cm^{-1} and the "dip" feature below this frequency are robust features independent of the value of q. Below 300 cm^{-1} however, the choice of q produces either a Drude-like feature or a finite energy mode which is consistent with Drude dynamics modified by localization.[49] The latter behavior is often seen in systems close to the metal-insulator transition in the presence of disorder.[63,64,65] We note that for a value of f obtained from the near-field image at a fixed temperature, the range of q values is highly constrained. Within EMT, percolation is predicted for $f \geq q$.[48] However, the far-field effective spectra and the

near-field patterns for $T = 342.6$ K indicate that percolation has not yet occurred and this means that $f < q$. Since solutions of eq.6 yielding a finite energy mode occur for $f \geq q$, we infer that these are unlikely to be correct, although they cannot be dismissed entirely. We also see that for $q > 0.34$, σ_{1a} turns negative over a finite frequency range and is unphysical. Hence, the spectra showing a narrow Drude-like mode centered at zero frequency are the most probable candidates for the optical constants of the metallic puddles.

The scattering rate $1/\tau(\omega)$ and the mass enhancement factor $m^*(\omega)/m_b$ of the metallic puddles obtained from the extended Drude analysis of the optical constants (see Appendix C) are plotted in Fig. 4(b),(c) for representative temperatures in the IMT regime. The scattering rate exhibits a gap-like form at low frequencies with an overshoot at ≈ 1000 cm^{-1}. We attribute the suppression of the scattering rate at low frequencies to partial gapping of the Fermi surface (i.e. a pseudogap). The connection between the suppression in the scattering rate and the opening of a pseudogap has been made earlier for the under-doped cuprates that are close to a Mott transition.[66,67,68] The pseudogap in VO_2 could be due to Mott physics, the Peierls instability[69] or a complex interplay between the two. We cannot rule out the possibility that this peculiar form of $1/\tau(\omega)$ and the "dip-hump" structure in $\sigma_1(\omega)$ are due to a low-lying interband transition.

Note that the mass enhancement factor of the metallic puddles increases substantially at low frequencies. The mass enhancement factor in the limit of $\omega \to 0$ diverges as one approaches the IMT with varying temperature (see inset of Fig. 4(c)). The mass divergence is likely due to electron-electron interactions and is a fingerprint of a Mott transition.[43,44] Note that our observation of mass divergence is not inconsistent with the first-order nature of the phase transition in VO_2 because about two-thirds of the entropy associated with the first-order transition is related to the lattice and the rest is electronic.[28] The relationship of electronic mass divergence and the electronic IMT to the structural transition needs to be explored in the future with nanoscale X-ray diffraction measurements of the metallic puddles.

As mentioned in the preceding paragraph, the form of the conductivity below 300 cm^{-1} is somewhat ambiguous. While the narrow Drude-like solutions show a variation in the low frequency conductivity, all such solutions lead to enhanced effective mass and an optical pseudogap in the metallic puddles within the extended Drude analysis. For solutions exhibiting a low energy mode, the reduced oscillator strength of this low-energy mode compared to that of the Drude mode in the rutile metal indicates enhanced optical effective mass.

Interfacial scattering and localization effects will become important when the size of the metallic puddles is comparable to or less than the intrinsic mean free path of the charge carriers within these puddles. Our estimate of the mean free path based on the scattering rate data in Fig. 4(b) is of the order of a few nanometers. The smallest puddles we can detect (limited by the 20 nm spatial resolution of our probe) are still in the regime where the mean free path is shorter than the spatial extent of metallic regions. Therefore, interfacial scattering and localization are unlikely to affect charge dynamics in the metallic puddles. However, we cannot rule out the possibility of quasiparticle localization which normally leads to a finite energy mode in the optical conductivity spectrum.

VII. SUMMARY AND OUTLOOK

We have performed far-field infrared ellipsometry and reflectance measurements on VO_2 films across the insulator-to-metal transition (IMT) and have determined the evolution of the effective optical constants. In addition, we have investigated the IMT with scanning near-field infrared microscopy and have directly observed the percolative phase transition. A combination of the far-field and near-field results within the ambit of the Bruggeman effective medium theory uncovers enhanced effective mass in the incipient metallic islands at the onset of the IMT. This result signifies the pivotal role of electronic correlations in the IMT physics.

We find that the dipole model of the near-field infrared contrast provides a satisfactory explanation of the observed amplitude contrast between the metallic puddles and the insulating regions. The agreement between experiment and the dipole model is evident only after the near-field amplitude from the metallic regions is normalized to the near-field amplitude from the insulating regions. Future s-SNIM experiments on VO_2 with Au reference should help better understand the evolution of the near-field amplitude as the sample goes through the IMT.

The methods and results reported here set a new standard for investigating the conducting state in other doped correlated insulators, for example the cuprates and manganites, where phase segregation is commonplace.[34,35,36,37,38,39] Ideally, one wants to obtain broad-band near-field infrared characterization on the nano-scale, without recourse to effective medium theory. The technology for this purpose is in its infancy and requires development.[71,72,73] Our work provides an incentive for such endeavors.

VIII. ACKNOWLEDGEMENTS

This work was supported by the U.S. Department of Energy Grant No.DE-FG03-00ER45799, the Deutsche Forschungsgemeinschaft Cluster of Excellence Munich Centre for Advanced Photonics, and the Electronics and Telecommunications Research Institute (ETRI), Korea.

IX. APPENDIX A

The measured ellipsometric coefficients $\Psi(\omega)$ and $\Delta(\omega)$ for $T = 342$ K are compared in Fig. 6a,b with the results from Bruggeman effective medium theory for an inhomogeneous two-phase system. The latter is a fit to the experimental data based on the optical constants of the monoclinic ($M1$) insulator and the rutile metal at $T =$ 360 K. The filling fractions and depolarization factor used for the fits are taken from Table I. Satisfactory agreement is obtained at higher frequencies (10000 - 20000 cm^{-1}) as can be seen clearly in the plots of the difference between the fits and the data displayed in the insets of Fig. 6a,b. However, the Bruggeman EMT should produce the most accurate results at low frequencies which is not the case here. This implies that the optical constants of the metallic phase in the inhomogeneous IMT regime may be different from those of the rutile metal at $T = 360$ K provided the optical constants of the $M1$ insulator do not change in the IMT regime.

X. APPENDIX B

Near-field amplitude images obtained while cooling the VO_2 film through the IMT are shown in Fig. 7. The images show that the insulating phase nucleates in the metallic host, and then proliferates and finally percolates. The IMT occurs about 8 K lower in temperature than on heating. Such a hysteresis is expected for a first-order phase transition and is seen in Fig.1b.

In Fig. 8a,b we demonstrate that repeated near-field imaging at fixed conditions yields unchanged patterns of metallic puddles. Imaging takes about 5 minutes (≈ 0.02 s per pixel of ≈ 15 nm $\times$ 15 nm size) and was immediately repeated. The reproducible patterns of metallic puddles rules out the possibility of slow dynamic fluctuations. If dynamic fluctuations occur on shorter time scales, then they do not affect the average pattern, especially they do not nucleate and stabilize into static metallic puddles.[70] We hypothesize that the specific patterns that emerge are most likely seeded and controlled by strain at the interface, defects, grain boundaries etc. These nucleation centers should lead to a reproducible pattern at a particular temperature, a feature that could not however be proven in the experimental setup because thermal drift due to thermal cycling through the phase transition prevented the repeated s-SNIM imaging of the same sample area.

We note here that simultaneous topography images were obtained along with near-field infrared images displayed in this work. We verified that the near-field infrared contrast between insulating and metallic regions in the IMT regime is due to the difference in optical constants and not due to topographic artifacts or changes in topography. However, we were unable to study our hypothesis that the metallic islands are seeded at grain boundaries, defects etc. This is because extensive image processing is required in order to identify the relationship between the new-born metallic islands and grain boundaries. This analysis can be reliably applied only if the topography data are more detailed. Optimized topography images will be required to investigate possible correlations between the nucleation sites of metallic islands and topographic features like grain boundaries.

XI. APPENDIX C

The following equations of the extended Drude formalism [49] describe the procedure for extracting the scattering rate $1/\tau(\omega)$ and the mass enhancement factor $m^*(\omega)/m_b$ from the real and imaginary parts of the complex optical conductivity of the metallic regions $\tilde{\sigma}_a(\omega)= \sigma_{1a}(\omega) + i\sigma_{2a}(\omega)$:

$$\frac{1}{\tau(\omega)} = \frac{\omega_p^2}{4\pi}\Big(\frac{\sigma_{1a}(\omega)}{\sigma_{1a}^2(\omega)+\sigma_{2a}^2(\omega)}\Big) \tag{7}$$

$$\frac{m^*(\omega)}{m_b} = \frac{\omega_p^2}{4\pi\omega}\Big(\frac{\sigma_{2a}(\omega)}{\sigma_{1a}^2(\omega)+\sigma_{2a}^2(\omega)}\Big) \tag{8}$$

The plasma frequency ω_p for the metallic states is obtained from the partial sum rule:

$$\frac{{\omega_p}^2}{8} = \int_0^{\omega_c} \sigma_{1a}(\omega)d\omega \tag{9}$$

Here, the upper frequency limit $\omega_c = 13700$ cm^{-1} is chosen for the rutile metal to exclude contributions from higher-lying optical transitions.[18,19] This gives $\omega_p = 22000$ cm^{-1} for the rutile metal and this value is nearly constant (within ten percent) for the metallic state in the nanoscale puddles with fixed $\omega_c = 13700$ cm^{-1}. With this nearly constant choice of the plasma frequency for all metallic states, the mass enhancement factor for the strongly correlated metallic puddles can be directly compared to the mass enhancement factor of the rutile metal.

The plasma frequency is related to the carrier density (n) and the band mass (m_b) by the following expression:

$${\omega_p}^2 = \frac{4\pi n e^2}{m_b} \tag{10}$$

We assume that the carrier density does not change significantly in the strongly correlated metallic puddles compared to the rutile metal.

* Email: mumtaz@physics.ucsd.edu

[1] N. F. Mott, *Metal-insulator transitions*, Taylor & Francis (1990).

[2] M. Imada, A. Fujimori, and Y. Tokura, Rev. Mod. Phys. **70**, 1039 (1998).

[3] R. Lopez, L. A. Boatner, and T. E. Haynes, R. F. Haglund Jr., and L. C. Feldman, Appl. Phys. Lett. **85**, 1410 (2004).

[4] M. M. Qazilbash, Z. Q. Li, V. Podzorov, M. Brehm, F. Keilmann, B. G. Chae, H. T. Kim, and D. N. Basov, Appl. Phys. Lett. **92**, 241906 (2008).

[5] T. Driscoll, S. Palit, M. M. Qazilbash, M. Brehm, F. Keilmann, Byung-Gyu Chae, Sun-Jin Yun, Hyun-Tak Kim, S. Y. Cho, N. Marie Jokerst, D. R. Smith, and D. N. Basov, Appl. Phys. Lett. **93**, 024101 (2008).

[6] M. Rini, A. Cavalleri, R. W. Schoenlein, R. Lpez, L. C. Feldman, R. F. Haglund Jr., L. A. Boatner, and T. E. Haynes, Optics Letters **30**, 558 (2005).

[7] M. Rini, Z. Hao, R. W. Schoenlein, C. Giannetti, F. Parmigiani, S. Fourmaux, J. C. Kieffer, A. Fujimori, M. Onoda, S. Wall, and A. Cavalleri, Appl. Phys. Lett. **92**, 181904 (2008).

[8] Bong-Jun Kim, Yong Wook Lee, Byung-Gyu Chae, Sun Jin Yun, Soo-Young Oh, and Hyun-Tak Kim, Appl. Phys. Lett. **90**, 023515 (2007).

[9] J. B. Goodenough, J. Solid State Chem. **3**, 490 (1971).

[10] C. J. Hearn, J. Phys. C: Solid State Phys. **5**, 1317 (1972).

[11] M. Gupta, A. J. Freeman, and D. E. Ellis, Phys. Rev. B **16**, 3338 (1977).

[12] H. Terauchi and J. B. Cohen, Phys. Rev. B **17**, 2494 (1978).

[13] R. M. Wentzcovitch, W. W. Schulz, and P. B. Allen, Phys. Rev. Lett. **72**, 3389 (1994); **73**, 3043 (1994).

[14] V. Eyert, Ann. Phys. (Leipzig) **11**, 650 (2002).

[15] H. W. Verleur, A. S. Barker Jr., and C. N. Berglund, Phys. Rev. **172**, 788 (1968).

[16] S. Shin, S. Suga, M. Taniguchi, M. Fujisawa, H. Kanzaki, A. Fujimori, H. Daimon, Y. Ueda, K. Kosuge, and S. Kachi, Phys. Rev. B **41**, 4993 (1990).

[17] K. Okazaki, S. Sugai, Y. Muraoka, and Z. Hiroi, Phys. Rev. B **73**, 165116 (2006).

[18] M. M. Qazilbash, K. S. Burch, D. Whisler, D. Shrekenhamer, B. G. Chae, H. T. Kim, and D. N. Basov, Phys. Rev. B **74**, 205118 (2006).

[19] M. M. Qazilbash, A. A. Schafgans, K. S. Burch, S. J. Yun, B. G. Chae, B. J. Kim, H. T. Kim, and D. N. Basov, Phys. Rev. B **77**, 115121 (2008).

[20] T. C. Koethe, Z. Hu, M. W. Haverkort, C. Schüßler-Langeheine, F. Venturini, N. B. Brookes, O. Tjernberg, W. Reichelt, H. H. Hsieh, H.-J. Lin, C. T. Chen, and L. H. Tjeng, Phys. Rev. Lett. **97**, 116402 (2006).

[21] P. B. Allen, R. M. Wentzcovitch, W. W. Schulz, P. C. Canfield, Phys. Rev. B **48**, 4359 (1993).

[22] V. J. Emery and S. A. Kivelson, Phys. Rev. Lett. **74**, 3253 (1995).

[23] M. M. Qazilbash, M. Brehm, Byung-Gyu Chae, P.-C. Ho, G. O. Andreev, Bong-Jun Kim, Sun Jin Yun, A. V. Balatsky, M. B. Maple, F. Keilmann, Hyun-Tak Kim, and D. N. Basov, Science **318**, 1750 (2007).

[24] H. T. Kim, B. G. Chae, D. H. Youn, S. L. Maeng, G. Kim, K. Y. Kang, and Y. S. Lim, New J. Phys. **6**, 52 (2004).

[25] H. T. Kim, Y. W. Lee, B. J. Kim, B. G. Chae, S. J. Yun, K. Y. Kang, K. J. Han, K. J. Yee, and Y. S. Lim, Phys. Rev. Lett. **97**, 266401 (2006).

[26] E. Arcangeletti, L. Baldassarre, D. Di Castro, S. Lupi, L. Malavasi, C. Marini, A. Perucchi, and P. Postorino, Phys. Rev. Lett. **98**, 196406 (2007).

[27] B.-J. Kim, Y. W. Lee, S. Choi, J.-W. Lim, S. J. Yun, and H.-T. Kim, T.-J. Shin, and H.-S. Yun, Phys. Rev. B **77**, 235401 (2008).

[28] A. Zylbersztejn and N. F. Mott, Phys. Rev. B **11**, 4383 (1975).

[29] D. Paquet and P. Leroux-Hugon, Phys. Rev. B **22**, 5284 (1980).

[30] T. M. Rice, H. Launois, and J. P. Pouget, Phys. Rev. Lett. **73**, 3042 (1994).

[31] S. Biermann, A. Poteryaev, A. I. Lichtenstein, and A. Georges, Phys. Rev. Lett. **94**, 026404 (2005).

[32] M. S. Laad, L. Craco, and E. Müller-Hartmann, Europhys. Lett. **69**, 984 (2005).

[33] E. Dagotto, Science **309**, 257 (2005).

[34] V. J. Emery, S. A. Kivelson, and J. M. Tranquada, Proc. Nat. Acad. Sci. USA **96**, 8814 (1999).

[35] M. Uehara, S. Mori, C. H. Chen, and S.-W. Cheong, Nature **399**, 560 (1999).

[36] L. Zhang, C. Israel, A. Biswas, R. L. Greene, and A. de Lozanne, Science **298**, 805 (2002).

[37] J. Lee, K. Fujita, K. McElroy, J. A. Slezak, M. Wang, Y. Aiura, H. Bando, M. Ishikado, T. Masui, J.-X. Zhu, A. V. Balatsky, H. Eisaki, S. Uchida, and J. C. Davis, Nature **442**, 546 (2006).

[38] Z. Sun, J. F. Douglas, A. V. Fedorov, Y.-D. Chuang, H. Zheng, J. F. Mitchell, and D. S. Dessau, Nat. Phys. **3**, 248 (2007).

[39] K. K. Gomes, A. N. Pasupathy, A. Pushp, S. Ono, Y. Ando, and A. Yazdani, Nature **447**, 569 (2007).

[40] F. Keilmann and R. Hillenbrand, Phil. Trans. R. Soc. Lond. A **362**, 787 (2004).

[41] H. S. Choi, J. S. Ahn, J. H. Jung, T. W. Noh, D. H. Kim, Phys. Rev. B **54**, 4621 (1996).

[42] P. U. Jepsen, B. M. Fischer, A. Thoman, H. Helm, J. Y. Suh, R. Lopez, and R. F. Haglund, Jr., Phys. Rev. B **74**, 205103 (2006).

[43] W. F. Brinkman and T. M. Rice, Phys. Rev. B **2**, 4302 (1970).

[44] H. T. Kim, Physica C **341-348**, 259 (2000).

[45] B. G. Chae, H. T. Kim, S. J. Yun, B. J. Kim, Y. W. Lee, D. H. Youn, and K. Y. Kang, Electrochem. Solid State Lett. **9**, C12 (2006).

[46] A. S. Barker Jr., H. W. Verleur, and H. J. Guggenheim, Phys. Rev. Lett. **17**, 1286 (1966).

[47] H. G. Tompkins and E. A. Irene, editors, Handbook of Ellipsometry, William Andrew Publishing/Springer Verlag (2005).

[48] G. L. Carr, S. Perkowitz, D. B. Tanner, Far infrared properties of inhomogeneous materials, Infrared and millimeter waves, vol. 13, edited by Kenneth J. Button (Academic Press, Orlando, 1985).

[49] D. N. Basov and T. Timusk, Rev. Mod. Phys. **77**, 721 (2005).

[50] S. V. Dordevic and D. N. Basov, Ann. Phys. (Leipzig) **15**, 545 (2006).

[51] S. Miyasaka, Y. Okimoto, and Y. Tokura, J. Phys. Soc.

Jpn. **71**, 2086 (2002).
[52] J. J. Tu, C. C. Homes, M. Strongin, Phys. Rev. Lett. **90**, 017402 (2003).
[53] B. Knoll, F. Keilmann, Nature **399**, 134 (1999).
[54] N. Ocelic, A. Huber, R. Hillenbrand, Appl. Phys. Lett. **89**, 101124 (2006).
[55] T. Taubner, F. Keilmann, and R. Hillenbrand, Optics Express **13**, 8893 (2005).
[56] M. B. Raschke and C. Lienau, Appl. Phys. Lett. **83**, 5089 (2003).
[57] Markus Brehm, Ph.D. Thesis (2006), Max-Planck-Institut für Biochemie, Martinsried, München, Germany.
[58] A. Cvitkovic, N. Ocelic and R. Hillenbrand, Optics Express **15**, 8550 (2007).
[59] M. A. Ordal, L. L. Long, R. J. Bell, S. E. Bell, R. R. Bell, R. W. Alexander Jr., and C. A. Ward, Applied Optics, **22**, 1099 (1983).
[60] J. Wu, Q. Gu, B. S. Guiton, N. P. de Leon, L. Ouyang, and H. Park, Nano Lett. **6**, 2313 (2006).
[61] Y. J. Chang, J. S. Yang, Y. S. Kim, D. H. Kim, T. W. Noh, D.-W. Kim, E. Oh, B. Kahng, and J.-S. Chung, Phys. Rev. B **76**, 075118 (2007).
[62] H. Zhan, V. Astley, M. Hvasta, J. A. Deibel, D. M. Mittleman, and Yong-Sik Lim, Appl. Phys. Lett. **91**, 162110 (2007).
[63] D. N. Basov, B. Dabrowski, and T. Timusk, Phys. Rev. Lett. **81**, 2132 (1998).
[64] M. Dumm, D. N. Basov, S. Komiya, Y. Abe, and Y. Ando, Phys. Rev. Lett. **88**, 147003 (2002).
[65] M. Dumm, S. Komiya, Y. Ando, and D. N. Basov, Phys. Rev. Lett. **91**, 077004 (2003).
[66] D. N. Basov, R. Liang, B. Dabrowski, D. A. Bonn, W. N. Hardy, and T. Timusk, Phys. Rev. Lett. **77**, 4090 (1996).
[67] A. V. Puchkov, P. Fournier, D. N. Basov, T. Timusk, A. Kapitulnik, and N. N. Kolesnikov, Phys. Rev. Lett. **77**, 3212 (1996).
[68] D. N. Basov, E. J. Singley, S. V. Dordevic, Phys. Rev. B 65, 054516 (2002).
[69] G. Gruner, Density waves in solids (Perseus Publishing, Cambridge, Massachusetts, 2000).
[70] L. D. Landau and E. M. Lifshitz, Vol. 5., Statistical Physics Part 1 (3ed., Pergamon, 1980).
[71] H.-G. von Ribbeck, M. Brehm, D.W. van der Weide, S. Winnerl, O. Drachenko, M. Helm, and F. Keilmann, Optics Express **16**, 3430 (2008).
[72] A. J. Huber, F. Keilmann, J. Wittborn, J. Aizpurua, and R. Hillenbrand, Nano Lett. **8**, 3766 (2008).
[73] P. Planken, Nature **456**, 454 (2008).

FIG. 1: (color online)(a) Room temperature X-ray diffraction data for the (200)-oriented $M1$-VO_2 film on ($\bar{1}012$)-oriented sapphire substrate. (b) The resistance of the VO_2 film is plotted while heating and cooling across the IMT. (c) Real part of the conductivity $\sigma_1(\omega)$ of VO_2 plotted as a function of frequency for various representative temperatures while heating the sample through the IMT. The open circle denotes the isosbestic (equal conductivity) point for all spectra. (Inset) The temperature dependence of the real part of the dielectric function ϵ_1 in the low-frequency limit ($\omega = 50$ cm^{-1}). (d) The optical constants of VO_2 as in (c) but with phonon contributions subtracted.

FIG. 2: (color online) Images of the near-field scattering amplitude s_2 (scale in relative units) over the same 4 μm by 4 μm area obtained by s-SNIM operating at the infrared frequency $\omega = 930$ cm^{-1}. The images were obtained for various temperatures while heating VO_2 through the IMT. The metallic regions depicted in light blue (light gray) and white give higher amplitude compared to the insulating phase shown in dark blue color (dark gray).

FIG. 3: (color online): (a) The distribution of near-field amplitude s_2 from images in Fig. 2 for selected temperatures. Note the log scale on the vertical axis for clarity of presentation. (b) the distribution of the normalized near-field amplitude for the same temperatures as in (a). The median near-field amplitudes for the insulating phase were used for normalizing the near-field amplitude in (b). The distributions plotted in panels (a) and (b) are the number of pixels normalized such that the area under each of the histograms is unity.

FIG. 4: (color online) Optical characterization of the metallic puddles derived from experiment: (a) the real part of the optical conductivity $\sigma_{1a}(\omega)$ (b) the scattering rate $1/\tau(\omega)$ and (c) the optical effective mass normalized by the band value $m*(\omega)/m_b$ of the metallic regions of VO_2 for representative temperatures in the IMT regime. The inset in (c) shows the $\omega \rightarrow 0$ limit of the mass enhancement factor as a function of temperature (data points between T = 400 K and 550 K are from Ref.18).

FIG. 5: (color online) Dependence of the real part of the optical conductivity $\sigma_{1a}(\omega)$ of the metallic puddles on the depolarization factor q, with f fixed at 0.31 for $T = 342.6$ K.

FIG. 6: Panels (a) and (b) display the ellipsometric coefficients $\Psi(\omega)$ and $\Delta(\omega)$ respectively that were measured for the VO_2 film on a sapphire substrate at $T = 342$ K (dashed gray curves). The thin black solid lines are the ellipsometric coefficients derived from the Bruggeman effective medium theory model as explained in Appendix A. The insets show the difference between the fits and the data for the respective ellipsometric coefficients.

FIG. 7: (color online) Near-field amplitude s_2 images (scale in relative units) obtained at $\omega = 930$ cm^{-1} with decreasing temperature through the IMT.

FIG. 8: (color online) Near-field amplitude s_2 images at $\omega = 930$ cm^{-1} at $T = 342$ K. Image (b) was obtained immediately after image (a).

Fig. 1

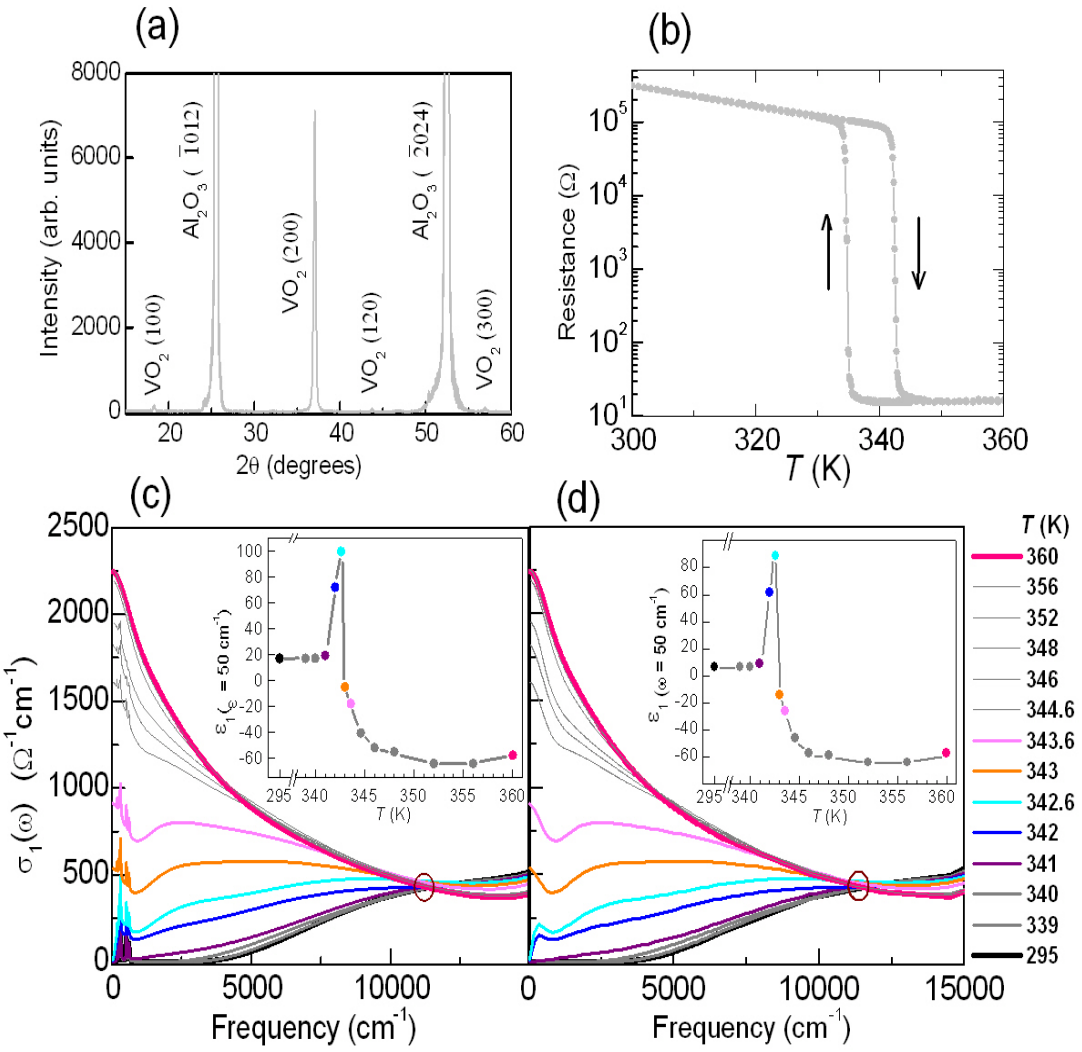

(a)
Intensity (arb. units)
2θ (degrees)
VO2 (100)
Al2O3 (1̄012)
VO2 (200)
VO2 (120)
Al2O3 (2̄024)
VO2 (300)
(b)
Resistance (Ω)
T (K)
(c)
(d)
σ1(ω) (Ω-1cm-1)
Frequency (cm-1)
ε1 (ω = 50 cm-1)
T (K)
T (K)
360
356
352
348
346
344.6
343.6
343
342.6
342
341
340
339
295

Fig. 2

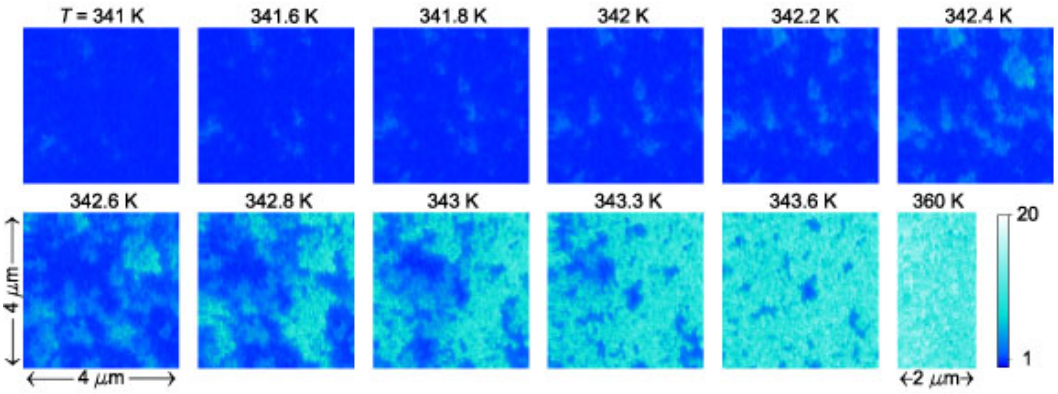

T = 341 K
341.6 K
341.8 K
342 K
342.2 K
342.4 K
342.6 K
342.8 K
343 K
343.3 K
343.6 K
360 K
20
1
4 μm
4 μm
2 μm

Fig. 3

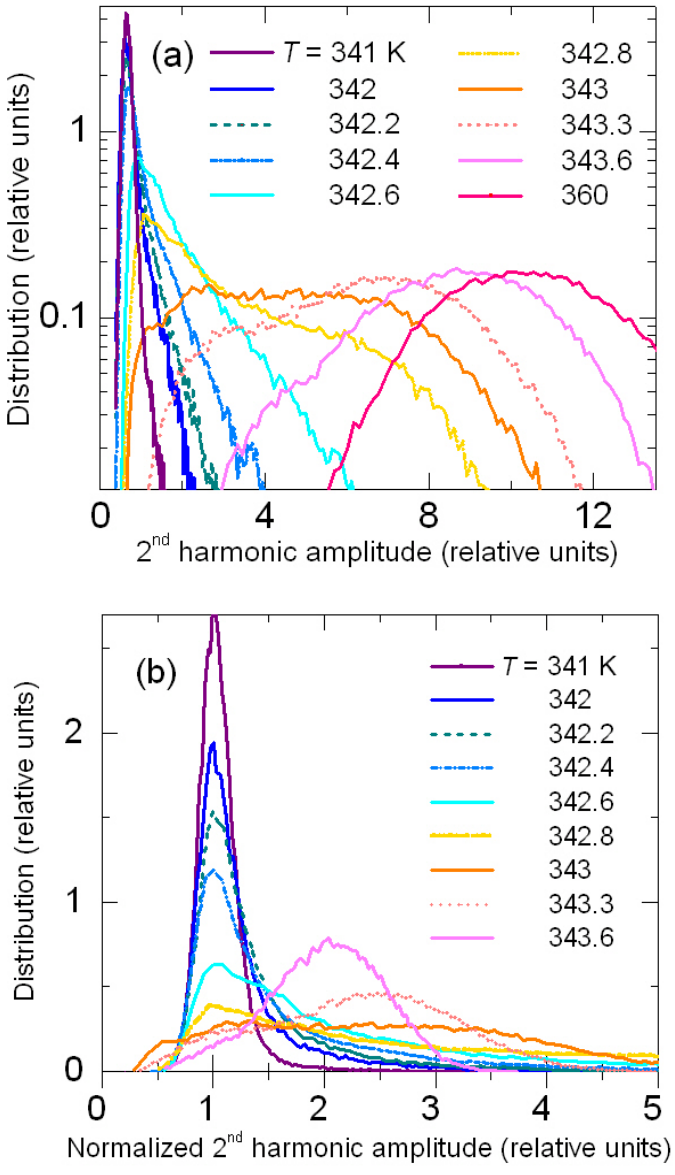

(a)
T = 341 K
342
342.2
342.4
342.6
342.8
343
343.3
343.6
360
Distribution (relative units)
1
0.1
0
4
8
12
2nd harmonic amplitude (relative units)
(b)
T = 341 K
342
342.2
342.4
342.6
342.8
343
343.3
343.6
Distribution (relative units)
2
1
0
0
1
2
3
4
5
Normalized 2nd harmonic amplitude (relative units)

Fig. 4

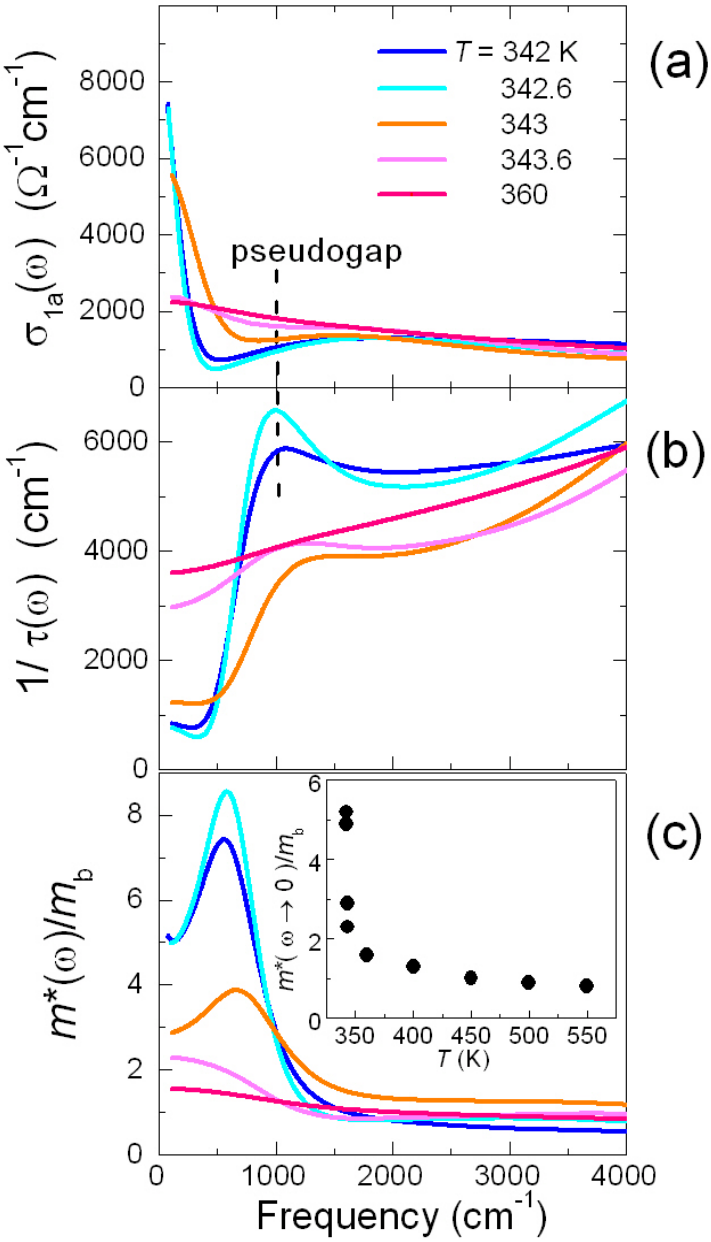

T = 342 K
342.6
343
343.6
360
pseudogap
(a)
(b)
(c)
σ1a(ω) (Ω-1cm-1)
1/ τ(ω) (cm-1)
m*(ω)/mb
m*(ω → 0)/mb
T (K)
Frequency (cm-1)

Fig. 5

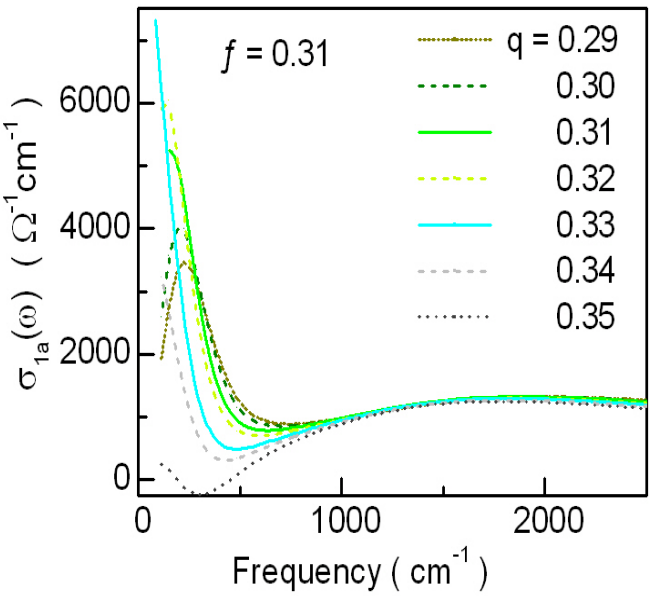

f = 0.31
q = 0.29
0.30
0.31
0.32
0.33
0.34
0.35
σ1a(ω) (Ω-1cm-1)
6000
4000
2000
0
0
1000
2000
Frequency (cm-1)

Fig. 6

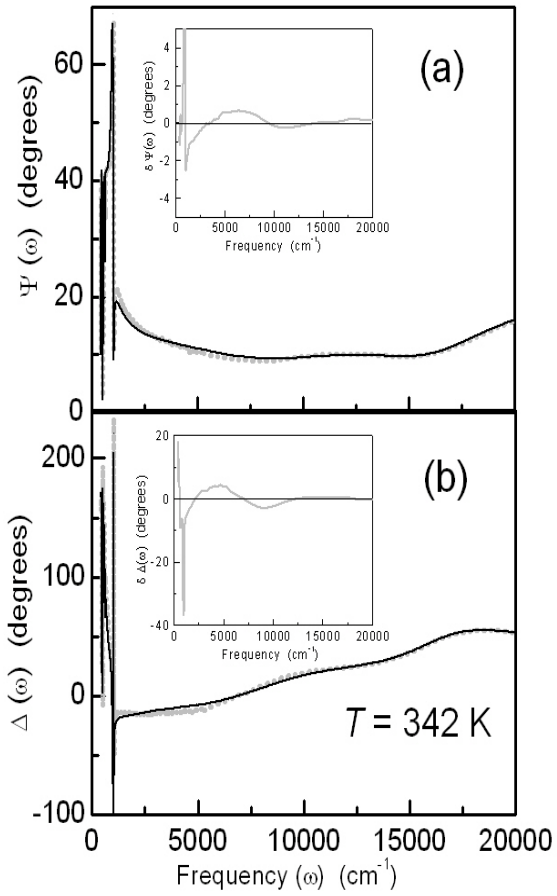

(a)
(b)
Ψ (ω) (degrees)
Δ (ω) (degrees)
δ Ψ(ω) (degrees)
δ Δ(ω) (degrees)
Frequency (ω) (cm-1)
Frequency (cm-1)
T = 342 K

Fig. 7

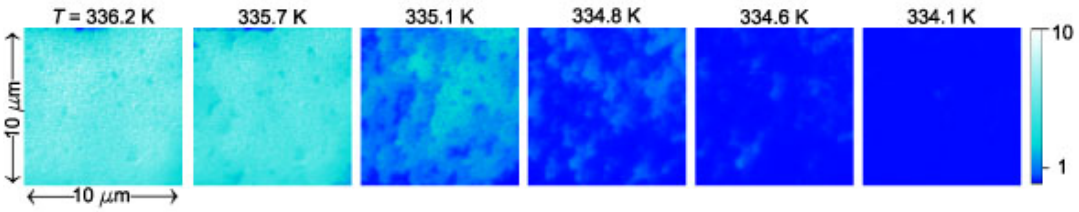


Fig. 8

